

## CALL FOR PAPERS | *Computational Analyses in Ion Channelopathies*

# A tale of two dogs: analyzing two models of canine ventricular electrophysiology

Elizabeth M. Cherry<sup>1,2</sup> and Flavio H. Fenton<sup>1,3</sup>

<sup>1</sup>Department of Biomedical Sciences, College of Veterinary Medicine, Cornell University, Ithaca; <sup>2</sup>Department of Physics and Astronomy, Hofstra University, Hempstead; and <sup>3</sup>The Heart Institute, Beth Israel Medical Center, New York, New York

**Cherry EM, Fenton FH.** A tale of two dogs: analyzing two models of canine ventricular electrophysiology. *Am J Physiol Heart Circ Physiol* 292: H43–H55, 2007. First published September 22, 2006; doi:10.1152/ajpheart.00955.2006.—The extensive development of detailed mathematical models of cardiac myocyte electrophysiology in recent years has led to a proliferation of models, including many that model the same animal species and specific region of the heart and thus would be expected to have similar properties. In this paper we review and compare two recently developed mathematical models of the electrophysiology of canine ventricular myocytes. To clarify their similarities and differences, we also present studies using them in a range of preparations from single cells to two-dimensional tissue. The models are compared with each other and with new and previously published experimental results in terms of a number of their properties, including action potential morphologies; transmembrane currents during normal heart rates and during alternans; alternans onsets, magnitudes, and cessations; and reentry dynamics of spiral waves. Action potential applets and spiral wave movies for the two canine ventricular models are available online as supplemental material. We find a number of differences between the models, including their rate dependence, alternans dynamics, and reentry stability, and a number of differences compared with experiments. Differences between models of the same species and region of the heart are not unique to these canine models. Similar differences can be found in the behavior of two models of human ventricular myocytes and of human atrial myocytes. We provide several possible explanations for the differences observed in models of the same species and region of the heart and discuss the implications for the applicability of models in addressing questions of mechanism in cardiac electrophysiology.

ionic models; ventricular arrhythmias; electrical alternans

OVER THE LAST SEVERAL DECADES, mathematical modeling and computer simulations of the electrophysiology of cardiac cells have become valuable tools for investigating electrical dynamics (6, 14, 22, 27, 34–36, 38, 43). The advantages of such studies include their reproducibility, the ease with which parameters can be varied, and control over certain experimental variables like noise and initial conditions. All have the potential to decrease the need for traditional experiments using animal cells and tissues. Simulations also allow access to all variables at all points in space, which is of particular importance when studying dynamics in three-dimensional tissue. Models and simulations are especially useful at providing insights into mechanisms. Because different scenarios can be modeled and simulated separately, with complete control over physiological conditions, the effects of parameter changes can be analyzed systematically.

As a result of the focus on model development, a large number of models of cardiac cellular electrophysiology representing an array of species and regions of the heart currently have been published (a few representative examples are Refs. 7, 9, 14, 16, 22, 27, 28, 31, 35, 36, 38, 40, 43, 47). Increases in computational power, especially with the rise of parallel computing, for the most part have eliminated issues associated with computational tractability of models in isolated cells, one-dimensional rings and cables, and two-dimensional tissues. Over the years, increased computational power, combined with the availability of more detailed biophysical data, have promoted increases in model complexity and have allowed the development of models that incorporate a broader range of electrophysiological properties, including memory, rate adaptation, and detailed intracellular calcium dynamics.

In some cases, different groups independently have developed models that describe the same region of the heart in the same species, giving rise to the question of whether the models are equivalent and, if not, under what conditions each model should be used. In this review, we will discuss two recent

Address for reprint requests and other correspondence: F. H. Fenton, Dept. of Biomedical Sciences, College of Veterinary Medicine, Cornell Univ., Ithaca, NY 14853 (e-mail: fhf3@cornell.edu).

cellular models of the electrophysiology of canine ventricular myocytes: the Fox-McHarg-Gilmour (FMG) model (22) and the Hund-Rudy (HR) model (27). The models contain many of the same currents, although these currents have different formulations with different conductances and dependencies on transmembrane voltage, intracellular calcium, and other ionic concentrations. The HR model also incorporates chloride currents, autophosphorylation through the  $\text{Ca}^{2+}$ /calmodulin-dependent protein kinase, and more complex calcium dynamics than the FMG model.

Because the FMG and HR models both were developed to describe the canine ventricular myocyte, it would be expected that the two models would possess similar properties. This paper reviews the similarities and differences between these two models. Their action potentials (APs), including the underlying transmembrane currents and ionic concentrations, are analyzed at both normal and fast pacing rates in single cells. In tissue, properties including upstroke rate of rise, rate adaptation, memory, conduction velocity, and alternans characteristics in one-dimensional (1d) cables are compared, along with the trajectories, dominant periods, and stability of reentrant spiral waves in two dimensions (2d). We find certain similarities between the properties of these models, but we also present many differences. When possible, we compare model properties with experimental data. In addition, we briefly review similar issues for two models of human ventricular and human atrial APs. Finally, we discuss the implications of disagreement among models of the same species and region for the usefulness of modeling and simulation in analyzing mechanisms of electrophysiological behavior.

#### CANINE VENTRICULAR CELL MODELS

The FMG and HR models include many of the same transmembrane currents, but there are a few exceptions. The FMG model includes a background sodium current ( $I_{\text{Na,b}}$ ), whereas the HR model includes a late sodium current ( $I_{\text{Na,L}}$ ), the  $\text{Na}^+$  current through the L-type  $\text{Ca}^{2+}$  channel ( $I_{\text{Ca,Na}}$ ), the transient outward chloride current ( $I_{\text{to2}}$ ), and a background chloride current ( $I_{\text{Cl,b}}$ ). In addition, intracellular calcium handling is more complex in the HR model, with separate variables tracking concentrations in the network and junctional sarcoplasmic reticulum (SR) and in the dyadic cleft; the inclusion of troponin buffering in the cytoplasm; and the incorporation of autophosphorylation through  $\text{Ca}^{2+}$ /calmodulin-dependent protein kinase. Intracellular  $\text{Na}^+$ ,  $\text{K}^+$ , and  $\text{Cl}^-$  concentrations are tracked as well in the HR model but not in the FMG model. Overall, the FMG model contains 13 variables and 13 transmembrane currents, whereas the HR model contains 29 variables and 16 transmembrane currents.

Along with the original model, we review an additional variant of the HR model for simulations in tissue. This was required because, in tissue, electrotonic currents decreased the action potential amplitude (APA) of the HR model to such a degree that the d-gate of the L-type calcium current ( $I_{\text{Ca}}$ ) failed to open, resulting in a slower, later, and longer-lasting current that prolonged AP durations (APDs) in tissue. Because these changes are needed primarily in tissue simulations, we refer to this variant of the HR model as the HRt model. However, we will review the properties of both the original HR and the HRt models in isolated cells and in tissue.

To restore  $I_{\text{Ca}}$  to a profile similar to that seen in the single HR cell, the following changes were made to obtain the HRt model (Y Rudy, personal communication). The sodium conductance ( $\bar{g}_{\text{Na}}$ ) was multiplied by 1.4 [which increased the amplitude of the  $\text{Na}^+$  current ( $I_{\text{Na}}$ )], the d-gate was raised to the nonvariable power of 1 in computing  $I_{\text{Ca}}$  (which facilitated  $I_{\text{Ca}}$  activation), and the gain of the  $\text{Ca}^{2+}$  release flux ( $I_{\text{rel}}$ ) was set to 1 (which eliminated the dependence of the size of the intracellular  $\text{Ca}^{2+}$  release on the magnitude of  $I_{\text{Ca}}$ ). In all other respects, the FMG and HR models were implemented as described in Refs. 22 and 27, respectively, with the stimulus current accounted for using the method of Ref. 26.

#### Transmembrane Currents and Their Rate Dependencies in Isolated Myocytes

Differences in model formulation between the FMG and HR models lead to differences in AP morphology and in the magnitudes of transmembrane currents and ionic concentrations. Figure 1 illustrates the membrane potential ( $V_m$ ), calcium transient ( $\text{Ca}_i$ ), and six of the most important currents for both the FMG model (dotted line) and the HR model (solid line) after 30 s of pacing at a cycle length (CL) of 500 ms. For clarity, only the original HR model and not the HRt model is shown; significant differences between the HR and HRt models are discussed below. When compared with the HR model, the FMG model has a lower resting membrane potential (RMP) ( $-95$  vs.  $-87$  mV), higher upstroke peak voltage ( $50$  vs.  $29$  mV), and larger APA ( $144$  vs.  $116$  mV). At this CL, both models have APs of similar duration, about 200 ms, and both have spike-and-dome morphology, although it is less pronounced for the HR model.  $\text{Ca}_i$  in the FMG model has a larger magnitude and a slightly different morphology than that of the HR model. When compared with the FMG model,  $I_{\text{Ca}}$  in the HR model is about twice as large in peak magnitude, is faster in reaching the maximum current, and replicates the spike-and-dome AP morphology. The exchanger current ( $I_{\text{NaCa}}$ ) is quite different for the two models: the FMG current is negative (inward) over most of the AP and is quick to reach steady state following the AP, whereas the HR current is positive (outward) until repolarization below  $-20$  mV and is slower to reach steady state during the diastolic interval (DI). Despite having similar peak magnitudes, the rapid component of the delayed rectifier  $\text{K}^+$  current ( $I_{\text{Kr}}$ ) has a different morphology in the two models, with the FMG model showing a sharper peak during repolarization and the HR model showing significant activity over much of the plateau as well. More similar currents include the slow component of the delayed rectifier ( $I_{\text{Ks}}$ ) (although the HR current is more than an order of magnitude larger), the transient outward current ( $I_{\text{to}}$ ) (at this CL), and the inward rectifier  $I_{\text{K1}}$  (with some differences during the plateau and during the DI). Between the HR and HRt models, the main differences at this CL are the increased upstroke amplitude and stronger  $I_{\text{Ca}}$  of the HRt model. These differences eliminate the spike-and-dome AP shape and lead to slight changes in the other currents due to the morphology change.

Both models exhibit alternans at short CLs, but different mechanisms appear to be involved. Figure 2 shows  $V_m$ ,  $\text{Ca}_i$ , and six currents for the FMG and HR models paced at a CL of 180 ms, for which both models exhibit alternans. Some cur-

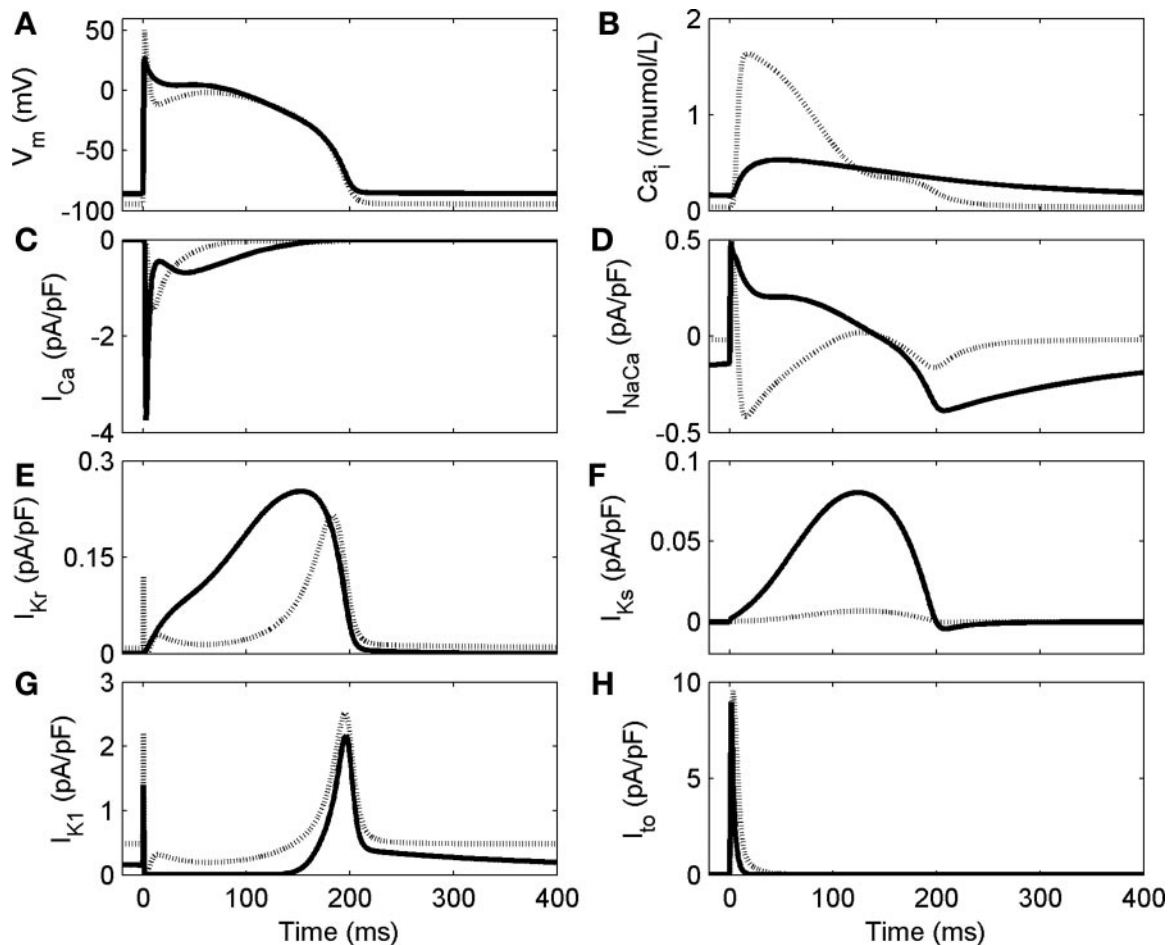


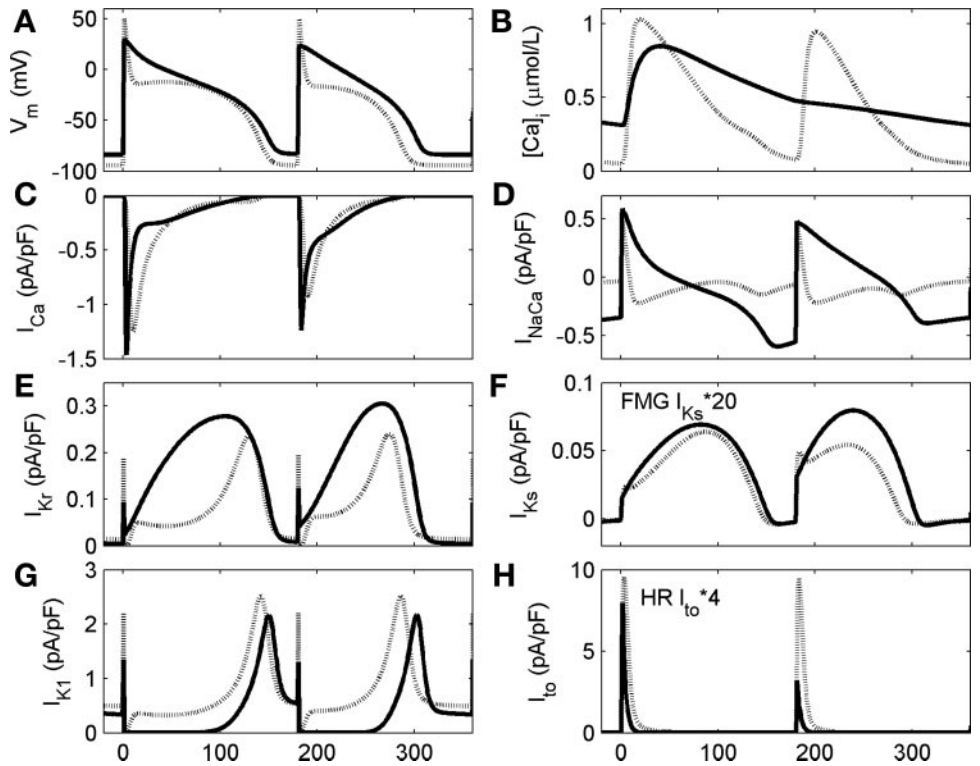
Fig. 1. Transmembrane potential ( $V_m$ ), intracellular calcium concentration ( $Ca_i$ ), and six transmembrane currents for the Fox-McHarg (FMG) model (dotted line) and the Hund-Rudy (HR) model (solid line). Data were obtained after the models were paced for 30 s at 500 ms with  $\Delta t = 0.01$  ms.  $I_{Ca}$ , L-type  $Ca^{2+}$  current;  $I_{NaCa}$ ,  $Na^+/Ca^{2+}$  exchanger current;  $I_{Kr}$ , rapid delayed rectifier  $K^+$  current;  $I_{Ks}$ , slowed delayed rectifier current;  $I_{K1}$ , inward rectifier current;  $I_{to}$ , transient outward current.

rents alternate strongly (such as  $I_{Ca}$ ), whereas others do not (such as  $I_{K1}$ ), and the two models often show different participation for the same currents. For instance,  $I_{to}$  in the HR model alternates quite noticeably, whereas it is essentially unchanged from the long to the short beat in the FMG model. One important difference in the models is that  $Ca_i$  in the FMG model alternates, whereas in the HR model it does not show an increase coincident with the short AP, as shown in Fig. 2B. This is because calcium release from the long AP has depleted the SR without enough time to replace SR calcium through uptake. For this reason, there is not enough SR calcium during the short AP to produce a substantial release current. The peak release current for the short AP is only 0.2% of its value during the long AP, which is insufficient to increase  $Ca_i$  during the second AP, leaving  $Ca_i$  to respond to pacing during alternans in almost a 2:1 manner. When compared with the HR model, the HRt model exhibits similar alternans behavior, with  $I_{Ca}$  and  $I_{to}$  alternating the most strongly. However, there is an important difference between HRt and the other two models. During alternans in the HRt model, the peak value of  $I_{Ca}$  is of opposite phase, so that peak  $I_{Ca}$  is larger during the short AP, and vice versa, as shown in Fig. 3.

#### APs in Tissue

APs in tissue generally are similar to those in isolated myocytes, as shown in Fig. 4, but some differences arise. The most notable is the prolongation of APD for the HR model in tissue because the electrotonic currents that bring neighboring cells to threshold as a wave of excitation propagates across a cell decrease the amplitude of that cell's upstroke substantially, a total of 24% in the HR model. This decrease occurs primarily through a decrease in the peak value of the upstroke from 28.7 to 0.7 mV at a CL of 1,000 ms (see Table 1). The decrease in amplitude prevents the d-gate that regulates  $I_{Ca}$  activation from opening, causing the channel to produce a later, slower, longer-lasting current instead of the primarily large, early, and rapid current produced in a single cell. This delayed current prolongs APDs, especially at shorter CLs. For comparison, the upstrokes of the FMG and HRt models also decrease significantly in tissue by 27 and 21% in tissue at the same CL, respectively. However, in these models the peak voltages remains high enough (10.8 and 11.5 mV, respectively) that all currents can be activated essentially in the same manner in which they are in a single cell, with some slight differences in repolarization for the FMG model.

Fig. 2. Currents during alternans for the FMG model (dotted line) and the HR model (solid line). Note that  $I_{Ks}$  for the FMG model has been multiplied by 20 and  $I_{to}$  for the HR model has been multiplied by 4 to facilitate comparison of the alternating currents. Data are shown after pacing at a cycle length (CL) of 180 ms for 30 s with  $\Delta t = 0.01$  ms.



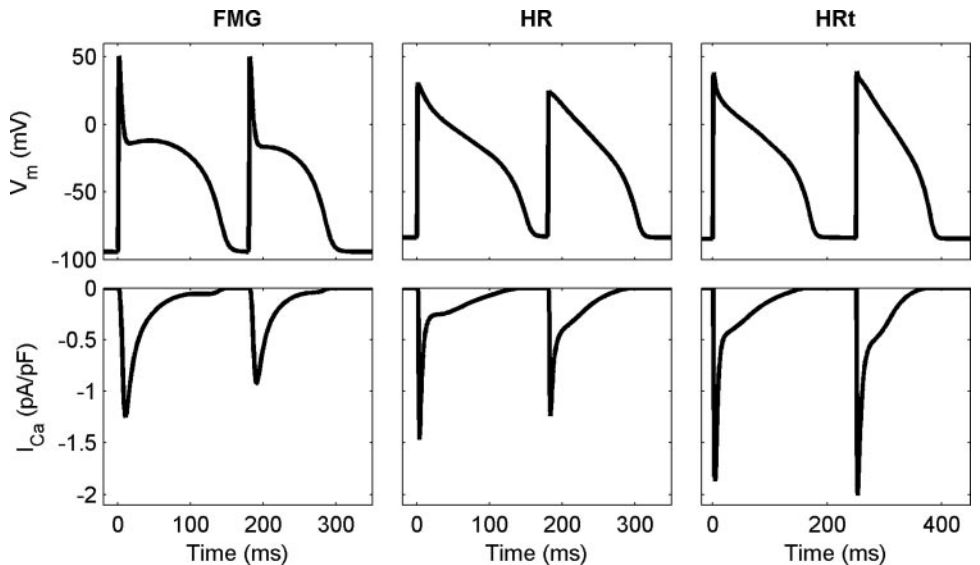
When compared with experimental values, the models generally achieve similar values of RMP, APA, and maximal upstroke rates of rise ( $dV/dt_{max}$ ) in tissue. All three models have slightly lower RMPs than those obtained in Refs. 5 and 15 for canine left ventricular (LV) epicardial tissue ( $-85.0$  and  $-84.2$  mV, respectively). The APAs of both the FMG and HRt models are close to experimentally obtained values of 98.3 ms (15) and 101.3 ms (5), whereas the HR model, as discussed, has an amplitude more than 10 ms smaller. The maximal upstroke velocity  $dV/dt_{max}$ , on the other hand, agrees well with experimental values of 151.8 V/s (15) and 154.5 V/s (5) only for the HRt model, the value of which is 155 V/s. The FMG and HR models have upstroke velocities of 211 and 117 V/s,

which are substantially higher and lower, respectively, than reported.

*Rate Dependence and Alternans*

The FMG and HR models overall respond differently to changes in rate, and for the HR model rate dependence can be substantially different in tissue compared with single cells. The CL dependence of the APD, obtained using the steady-state protocol of Ref. 30 after 30 s of pacing using twice diastolic threshold current, is shown in Fig. 5, A–F, for the FMG, HR, and HRt models for both single cells and one-dimensional cables. The FMG model in a single cell and the HRt model in

Fig. 3. Alternans in voltage and  $I_{Ca}$  for the FMG, HR, and HRt models in single cells. For the FMG and HR models, the larger magnitude of  $I_{Ca}$  corresponds to the longer action potential (AP), but for the HRt model this is reversed. CLs are 180 ms for the FMG and HR models and 250 ms for the HRt model. Note that the time scale for the HRt model is slightly different to accommodate its longer CL. Data are shown after pacing for 30 s with  $\Delta t = 0.01$  ms.



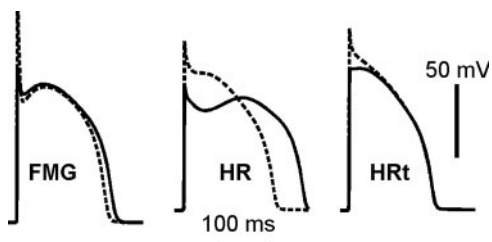


Fig. 4. APs of the three models in tissue (solid line) and in single cells (dashed line) at a CL of 500 ms, with  $\Delta t = 0.01$  ms and  $\Delta x = 0.0125$  cm.

a single cell and in tissue all show a transition from 1:1 behavior to 2:2 (alternans) and back to 1:1 at short CLs. In contrast, the HR model in a single cell and the FMG model in tissue do not transition back to 1:1 behavior from alternans. The FMG model in tissue loses the second region of 1:1 dynamics at short CLs because propagation is not possible at these CLs, so the tissue transitions from 2:2 dynamics to 2:1, where only every other beat generates a propagating AP. In addition, the alternans onset also is shifted to occur 15 ms earlier. For the HR model, the alternans disappears entirely in tissue. Although this effect has been observed before and explained as a combination of memory and electrotonic effects (11), in this case the difference occurs because the model itself has completely different restitution curves in tissue (see Fig. 5, *H* and *K*) as a result of the decrease in AP amplitude, which affects  $I_{Ca}$  dynamics. The HRt model qualitatively exhibits similar dynamics in an isolated myocyte and in tissue; however, the alternans onset in one dimension occurs 40 ms earlier than in a single cell, and the offset similarly is shifted 45 ms earlier. These differences are summarized in Table 1.

**Rate dependence and alternans in isolated myocytes.** When compared with experimental data from myocytes isolated from canine LV epicardium, all the model APDs at a CL of 1 s (208, 245, and 229 ms, respectively, for the FMG, HR, and HRt models) are similar to experimentally observed values between 220 and 250 ms (5, 32, 33), as are APDs at a CL of 300 ms [175, 166, and 158 ms, respectively, compared with about 165 ms in experimentally isolated myocytes (32, 33)]. When compared with canine LV epicardial tissue preparations, model APDs generally are at or beyond the long end of reported values of APD. At a CL of 1 s, APDs typically are around 210 to 225 ms (1, 5, 32) compared with 224, 254, and 232 ms, respectively, for the FMG, HR, and HRt models in tissue. Although the FMG model APD is closest to experiments at a CL of 1 s, it has not shortened as much as experiments by a CL of 300 ms. Experimentally, APDs of 125 to 175 ms are seen at this CL (5, 15, 32), closer to the value obtained for the HR model (151 ms). Whereas the HRt model APD also shortens appreciably as the rate is increased, it alternates by a CL of 300 ms, which generally is not observed experimentally (1, 5, 32).

All three models exhibit similar alternans magnitudes in a single cell with maximum values of 36, 35, and 40 ms and average values of 25, 32, and 32 ms for the FMG, HR, and HRt models, respectively. The range of CLs exhibiting alternans (alternans range) is 55 ms for the FMG model and larger for both the HR (65 ms) and HRt (85 ms) models. The alternans onset CLs are quite different, however, with the onsets occurring at 205, 235, and 280 ms, respectively, for the FMG, HR, and HRt models.

**Rate dependence and alternans in tissue.** In tissue, additional differences emerge. The alternans range of the FMG model decreases sharply from 55 to 20 ms because of the large increase in the CL at which 2:1 block occurs, whereas the magnitude increases in tissue from an average value of 25 to 50 ms and a maximum value of 36 to 67 ms. The HRt model, in contrast, retains a similar alternans range (80 ms) and slightly larger maximum and average magnitudes (38 and 53 ms, respectively) compared with the single cell case. In tissue, therefore, the HRt model has an alternans range four times that of the FMG and an average alternans magnitude 25% smaller. The alternans onset CLs also are shifted higher compared with the single cell case, from 205 to 220 ms for the FMG model and from 280 to 320 ms for the HRt model. As mentioned above, the HR model does not show alternans in tissue.

We also compared our alternans-related findings by using the FMG and HRt models in tissue with properties we obtained by microelectrode studies using thin canine epicardial and endocardial tissue slices (see Fig. 6) using the same protocols described in Ref. 30. The alternans onset in the FMG model was 220 ms, nearly halfway between the epicardial (200 ms) and endocardial (256 ms) experimental onset data (see Table 2), and for the HRt model was 320-ms substantially higher than the experiments. The transition to 2:1 block occurred at a relatively high CL in the FMG model (200 ms) compared with experiments (137 and 158 ms in epicardium and endocardium, respectively), whereas the HRt model achieved a better match,

Table 1. Properties of the FMG, HR, and HRt models in single cells (0d) and in tissue (1d)

	FMG		HR		HRt	
	0d	1d	0d	1d	0d	1d
RMP at 1 s, mV	-94.4	-94.3	-86.9	-86.8	-86.9	-86.9
Upstroke peak at 1 s, mV	49.8	10.8	28.7	0.6	38.3	11.5
AP amplitude at 1 s, mV	144.2	105.1	115.6	87.4	125.2	98.4
APD <sub>90</sub> threshold at 1 s, mV	-79.9	-83.8	-75.3	-78.0	-74.4	-77.0
2:2 onset, ms	205	220	235	N/A	280	320
2:2 offset (before 1:1), ms	150	N/A	N/A	N/A	195	240
2:1 onset, ms	85	200	170	150	135	150
Alternans range, ms	55	20	65	N/A	85	80
Maximum alternans magnitude, ms	36	67	35	N/A	40	53
Average alternans magnitude, ms	25	50	32	N/A	32	38
Memory amplitude (range of APD <sub>max</sub> in S1-S2 protocols), ms	34	17	15	203	65	73
dV/dt <sub>max</sub> (tissue only), V/s		211		117		155
CV <sub>max</sub> (tissue only), cm/s		49		46		52

Alternans is defined as occurring when the action potential duration (APD) alternates between successive beats by at least 2 ms. The 2:2 and 2:1 onset values are the first cycle lengths (CLs) showing these behaviors, whereas the 2:2 offset is the last CL with alternans before resuming 1:1 behavior and is not applicable in every case. These onsets and offsets are determined within 5 ms in zero dimension (0d) and 10 ms in one dimension (1d); similarly, alternans magnitudes are determined at 5- and 10-ms intervals within the region of alternans in 0d and 1d, respectively. The range of maximal APD (APD<sub>max</sub>) in S1-S2 protocols is determined by using the average value of the difference for diastolic intervals >500 ms. The values of maximal upstroke rate of rise (dV/dt<sub>max</sub>) are determined only in tissue to eliminate the effects of stimulus magnitude and are measured after 30 s of pacing at a CL of 1 s. FMG, Fox-McHarg-Gilmour; HR, Hund-Rudy; HRt, tissue simulation of HR model; RMP, resting membrane potential; AP, action potential; CV<sub>max</sub>, maximal conduction velocity; N/A, not applicable.

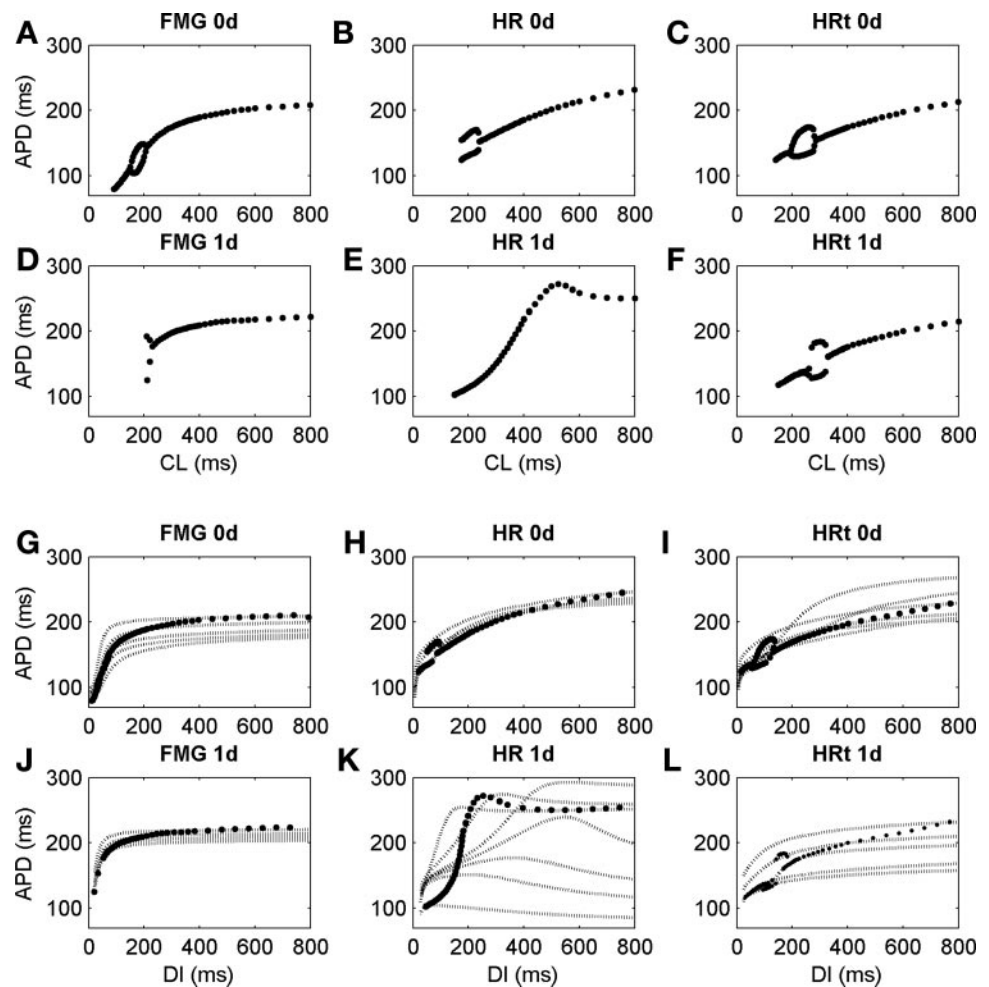


Fig. 5. Rate adaptation and restitution of AP duration (APD) for the FMG, HR, and HRt models in a single cell (0d, zero dimension) and 1 cm away from the stimulus site in a 1.25 cm-long cable (1d, one dimension). A–F: steady-state rate adaptation was measured after 30 s of steady-state pacing at each CL shown. Note that the HR and HRt models continued to adapt for longer than 60 s and did not reach a steady state during that time. G–L: steady-state (filled circles) and S1–S2 (dotted lines) restitution curves for the FMG, HR, and HRt models in single cells and in a 1d cable. The values of S1 are listed from longest to shortest APD at the longest S2 value tested. G: S1 values are 800, 400, 210, 145, and 90 ms. H: S1 values are 1,000, 600, 240, and 300 ms. I: S1 values are 190, 180, 1,000, 600, 140, and 300 ms. J: S1 values are 1,000, 400, 300, and 230 ms. K: S1 values are 340, 400, 800, 330, 320, 300, and 150 ms. L: S1 values are 1,000, 600, 330, 230, and 150 ms. APDs were determined using a fixed voltage threshold corresponding to  $APD_{90}$  at a CL of 1,000 ms (specific values are given in Table 1). In all cases,  $\Delta t = 0.01$  ms,  $\Delta x = 0.0125$  cm, and the diffusion coefficient ( $D$ ) =  $0.001$   $\text{cm}^2/\text{s}$ .

with 2:1 behavior beginning at 150 ms. The overall range of CLs that exhibited alternans was low in the FMG model (20 ms) but for the HRt model (80 ms) was close to the experimental values of 63 and 98 ms, respectively. Alternans magnitudes in both models (averages of 50 and 38 ms for FMG and HRt, respectively) were much larger than in experiments (4 and 9 ms for epicardial and epicardial tissue, respectively). These comparisons indicate that the FMG model appears to better match experimental data for the alternans onset CL (Fig. 5D), whereas the HRt model better matches the 2:1 onset and alternans CL range (Fig. 5F). The bifurcation of the APD rate dependence, on the other hand, generally is more gradual in experiments than in the models, suggesting that a border-collision bifurcation may be a better characterization of alternans in tissue (48) than the typical pitchfork bifurcation produced by models. Neither model reproduces the bifurcation characteristics well.

**Crossing of APs during alternans.** The HRt model in tissue also was able to reproduce another property observed experimentally during alternans: the crossing of superimposed long and short APs during alternans (see Fig. 6D). Two possible explanations for this crossing are the rate dependence of  $I_{to}$  and the rate dependence of  $I_{Ca}$  in the HRt model.  $I_{to}$  has a slow recovery from inactivation that results in a small current following a short DI, so that the smaller value of  $I_{to}$  is coincident with the short AP during alternans. The reduction in

$I_{to}$  may be responsible for the initially higher voltage of the short AP, but other currents that give rise to the shorter AP repolarize the cell more quickly than during the long AP so that a crossing occurs. The large  $I_{Ca}$  coincident with the short AP also may result in the initially higher voltage of the short AP. It is also possible that both currents are involved to produce the crossing of the APs. In contrast, the FMG model, with its pairing of large  $I_{Ca}$  with the long AP during alternans and its lack of rate dependence of  $I_{to}$ , does not produce APs that cross during alternans.

#### Short-Term Memory

Cardiac tissue has short-term memory associated with accommodation to changes in CL (11, 19, 23), as well as long-term memory associated with remodeling that occurs over days to weeks (39), which we do not consider here. In the absence of short-term memory, S1–S2 restitution curves with different S1 CLs would be the same. However, these models possess a memory of pacing history and therefore are not purely dependent on the previous DI, with the result that S1–S2 restitution curves are dependent on the choice of S1. One measure of memory that we propose here is the range of  $APD_{max}$  at long DIs for various S1 CLs, which we refer to as the memory amplitude. With the use of this measure, the memory properties of the models, like their alternans proper-

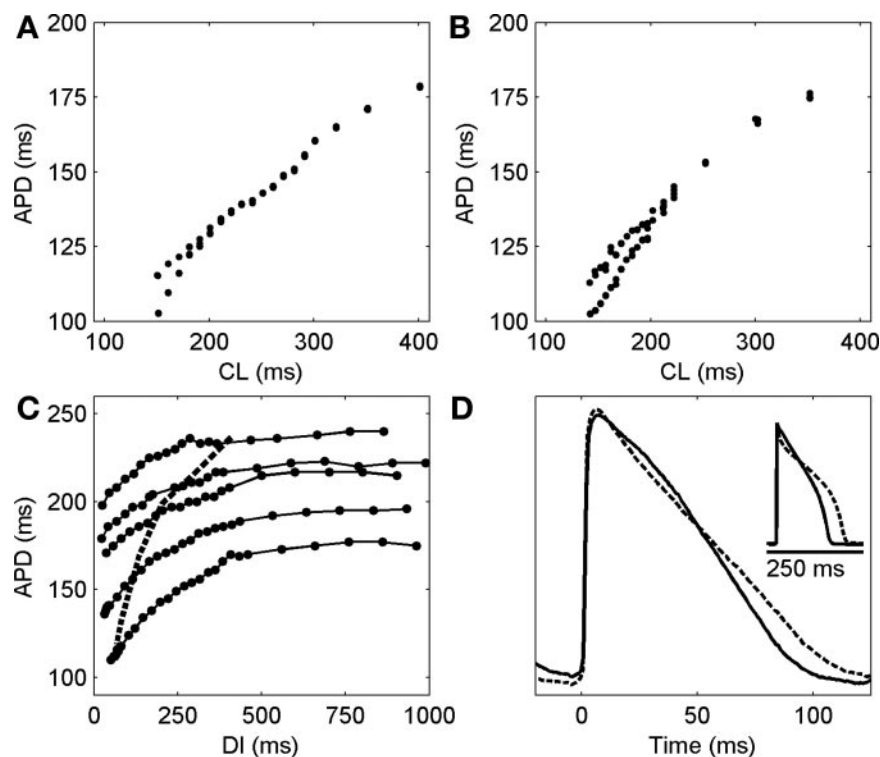


Fig. 6. Experimental rate adaptation data from canine ventricular epicardial and endocardial preparations. *A*: representative rate adaptation in ventricular epicardial tissue. *B*: representative rate adaptation in ventricular endocardial tissue. *C*: representative S1-S2 restitution curves (solid with filled circles) and the steady-state restitution curve (dashed) for ventricular endocardial tissue. S1 values, from top to bottom, are 650, 500, 400, 300, and 200 ms. *D*: superimposed representative long and short APs from the endocardium at a CL of 130 ms. The short and long APs cross during repolarization. *Inset*: similar crossing of long and short APs from the HRT model in a single cell at a CL of 250 ms.

ties and rate dependencies, are different, both quantitatively and qualitatively. S1-S2 restitution curves of the three models for different values of the S1 CL are shown with dotted lines in Fig. 5, *G–L*, along with the steady-state curves shown with solid lines for both isolated cells and tissue. The FMG model exhibits a straightforward dependence on S1, with APDs at all values of S2 decreasing with S1 (see Fig. 5, *G* and *J*). The memory amplitude is 34 ms in a single cell and half that, 17 ms, in tissue. The main reason for the decreased memory amplitude in tissue is that the CL at which 2:1 block is reached has changed from 85 ms in a single cell to 200 ms, thereby preventing the use of short S1 CLs that give rise to a large portion of the memory effects. In the HR model, S1-S2 restitution curves have a more complex dependence on the value of S1. In a single cell, these curves cross each other so that the curve with the longest APD changes over time. For instance, as shown in Fig. 5*H*, at the longest DI, APDs from longest to shortest correspond to S1 CLs of 1,000, 600, 240, and 300 ms. This order changes to 1,000, 240, 600, and 300 ms

Table 2. Experimentally observed properties of canine ventricular epicardium and endocardium

	Epicardium	Endocardium
2:2 onset, ms	200.0 ± 20.0 ( <i>n</i> =3)	255.9 ± 35.2 ( <i>n</i> =17)
2:1 onset, ms	136.7 ± 5.8 ( <i>n</i> =3)	157.6 ± 31.2 ( <i>n</i> =17)
Alternans range, ms	63.3 ± 15.3 ( <i>n</i> =3)	98.3 ± 45.0 ( <i>n</i> =17)
Maximum alternans magnitude, ms	8.1 ± 4.2 ( <i>n</i> =3)	15.6 ± 9.7 ( <i>n</i> =17)
Average alternans magnitude, ms	4.3 ± 1.4 ( <i>n</i> =3)	9.4 ± 8.3 ( <i>n</i> =17)
Memory amplitude (range of APD <sub>max</sub> in S1-S2 protocols) ms		54.6 ± 32.1 ( <i>n</i> =5)

Alternans is defined as occurring when the APD alternates between successive beats by at least 2 ms. S2-S2 restitution curves were obtained only in endocardium. *n*, number of samples.

at a DI of 400 ms and to 1,000, 600, 300, and 240 ms at the shortest DI values. Nevertheless, overall the memory amplitude is only 15 ms. The small memory amplitude occurs in part because the APD<sub>max</sub> decreases to a minimum for S1 CL = 300 ms and then increases. In tissue, the memory amplitude increases to 203 ms because of the changes in AP morphology that occur as a function of CL. Although the APD<sub>max</sub> primarily decreases with S1 CL, the region of negative slope on the restitution curve dictates that the S1-S2 restitution curves at long S1 CLs cross each other. Therefore, as shown in Fig. 5*K*, although at large DIs the APD<sub>max</sub> for the largest S1 CLs decrease in the order 340, 400, and 800 ms, at a DI of 200 ms the order has reversed to 800, 400, and 340 ms. The HRT model exhibits the most memory in a single cell, an amplitude of 65 ms, but also has a complex dependence on the value of S1 used. Figure 5*I* shows that at the longest DI, curves from longest to shortest APD are 190, 180, 1,000, 600, 140, and 300 ms S1 CLs, but at a DI of 400 ms, the order changes to 190, 1,000, 180, 600, 300, and 140 ms, and at the shortest DIs the order is 1,000, 600, 140, 300, 180, and 190 ms. The complex dependence in the HRT model becomes straightforward in tissue, with APDs proceeding from longest to shortest as S1 CL is decreased and a memory amplitude of 73 ms, as shown in Fig. 5*L*. Overall, in single cells, the HR and HRT models have 0.44 and 1.9 times the memory amplitude of the FMG model, respectively, and in tissue, the HR and HRT models have 12 and 4.3 times the memory amplitude of the FMG model.

A summary of AP and rate dependence characteristics for all three models in single cells and tissue is given in Table 1. In addition, because of memory effects, the values in Table 1 for the HR and HRT models are sensitive to pacing history. For example, when paced for 5 s at each CL instead of 30 s, the

HRt alternans onset becomes 220 ms, 2:1 block occurs at 180 ms, and the maximum and average alternans amplitudes decrease to 31 and 20 ms, respectively, in a single cell. Further changes occur if pacing at each CL persists for a longer time. Thus, the HR and HRt models may require substantially longer times to reach a completely steady state for every CL than the FMG model.

We also compared restitution and memory properties with our experimental findings by using canine epicardial and endocardial tissue. With the use of an S1 CL of 1 s, APDs of 219 and 216 ms for the FMG and HRt models, respectively, were similar to a reported value of 220 ms (5) using a DI of 300 ms; the APD of 250 ms for the HR model was substantially longer. At the smallest DI values, the minimum APDs obtained for the FMG, HR, and HRt models were 154, 114, and 148 ms, respectively, all of which were lower than the experimental minimum APD of 190 ms (5). Different S1-S2 restitution curves for a range of values of S1 were obtained in our lab only in endocardial preparations and, as shown in Table 2, resulted in a range of APD<sub>max</sub> of 55 ms, in between the model values of 17 ms for the FMG model and 73 ms for the HRt model, so that neither model reproduces the APD<sub>max</sub> range in S1-S2 protocols well. However, the APDs obtained for each DI decreased with S1 CL in a straightforward manner in experiments (Fig. 6C), more like the FMG model (Fig. 5J) than the HRt model (Fig. 5L).

#### Splitting of Steady-State Restitution Curves

The steady-state restitution curves, shown as solid lines in Fig. 5, G–L, are different for the three models, with the notable property that the restitution curves split in regions where alternans occur. Whereas the splitting of the APD restitution curve as a function of CL, as shown in Figs. 5, G–I, and L, is an expected characteristic during alternans (25), splitting of the restitution curve as a function of DI is not. The splitting regions are especially easy to observe for the HR model in an isolated cell and for the HRt model in cells and in tissue; however, it also occurs to a lesser degree for the FMG model in an isolated cell.

To date, steady-state restitution curves always have been considered single-valued functions of DI, except during discordant alternans in a one-dimensional cable or ring due to electrotonic effects (45). However, for the cases shown in Fig. 5, the splitting does not occur during discordant alternans, because the simulated cables are small and only support concordant alternans, but instead occurs because of memory. In these models, memory makes the APD a function not only of DI but of previous APDs and DIs, thereby allowing the restitution curve to be bivalued for DI and producing split regions of restitution. In these regions the slope of each APD restitution branch can have any slope (either steep or flat), and the only requirement is that for every CL that produces alternans, the slope connecting the two alternating points must be one. Therefore, once splitting by memory is present, the restitution curve does not need to have a slope greater than one to have alternans, as shown in the case of the HR model in a single cell (Fig. 5H). Here, the slope of the steady-state restitution curve before the alternans region is 0.28, and during alternans the maximum slope of the upper branch is 0.5 and that of the lower branch is 0.3. This is significant because it

demonstrates that a steep restitution curve is not necessary for alternans to occur and can potentially explain experimental results where alternans are observed in regions where the slope of the restitution curve is  $<1$  (24).

#### Conduction Velocity Restitution

All three models exhibit extremely limited restitution of conduction velocity (CV) as determined in a one-dimensional cable using the same protocols as for APD restitution. The maximum CV values are similar among the three models: 49, 46, and 52 cm/s for the FMG, HR, and HRt models, respectively, with the CV decreasing  $<2$  cm/s over the entire range of DIs  $>20$ , 30, and 35 ms, respectively. The maximal CV of the HRt model is increased 13% compared with the HR model because the increased sodium conductance contributes to faster propagation speeds. The values of  $dV/dt_{\max}$  vary over almost a factor of two among the three models, indicating that the CV is not determined by this value but rather by the entire upstroke. The value of  $dV/dt_{\max}$  for the HRt model is 1.3 times that of the HR model, a difference that again arises from the increased sodium conductance and quantitatively is almost the same magnitude (the HRt conductance is 1.4 times that of the HR model).

#### Reentrant Spiral Waves

In tissue, the dynamics of spiral waves in large domains were compared after initiation using a cross-field stimulation protocol, with tip trajectories computed using the zero normal velocity method (18). The FMG model produced stable spiral wave dynamics with a strongly linear core, as shown in Fig. 7, A and E. The model experienced short-lived transient breakup for about 2.2 s after initiation of the spiral wave, after which it stabilized with a meandering linear core that became a slowly processing stable pattern from about 4.5 s after initiation and lasted until the end of the simulation, about another 20 s. The HR model, on the other hand, produced a hypermeandering trajectory that could be stable or could break up depending on the initial conditions used. Figure 7B shows a stable spiral wave with a hypermeandering core (as shown in Fig. 7E), but applying the S2 stimulus that initiated the spiral wave 30 ms earlier led to sustained breakup, as shown in Fig. 7C. This sensitivity of reentry stability to initial conditions has been shown previously to arise from regions of bistability for a given CL (20, 25), where a 1:1 or a 2:2 response can coexist with a 2:1 response. The two branches of response can be accessed by different initial conditions or by a Doppler shift produced by the meander or hypermeander of a reentry (20). In contrast, the HRt model, with its faster CV compared with the HR model, produced more sustained quasi-breakup because of an increase in wave front-back interactions (Fig. 7D). Most of the wave breaks that occurred healed quickly, within tens of milliseconds, although several longer-lasting breaks leading to more persistent additional spiral waves occurred occasionally.

A fairly stable section of the tip trajectory trace, when only one wave was present in the domain, shows that the HRt model spiral wave meandered much more strongly than spiral waves in either the FMG or HR models (Fig. 7E). However, the length of the linear petals is fairly similar for all three models, about 3–5 cm. The dominant spiral periods varied among the models, with that of the FMG model the smallest, around 120

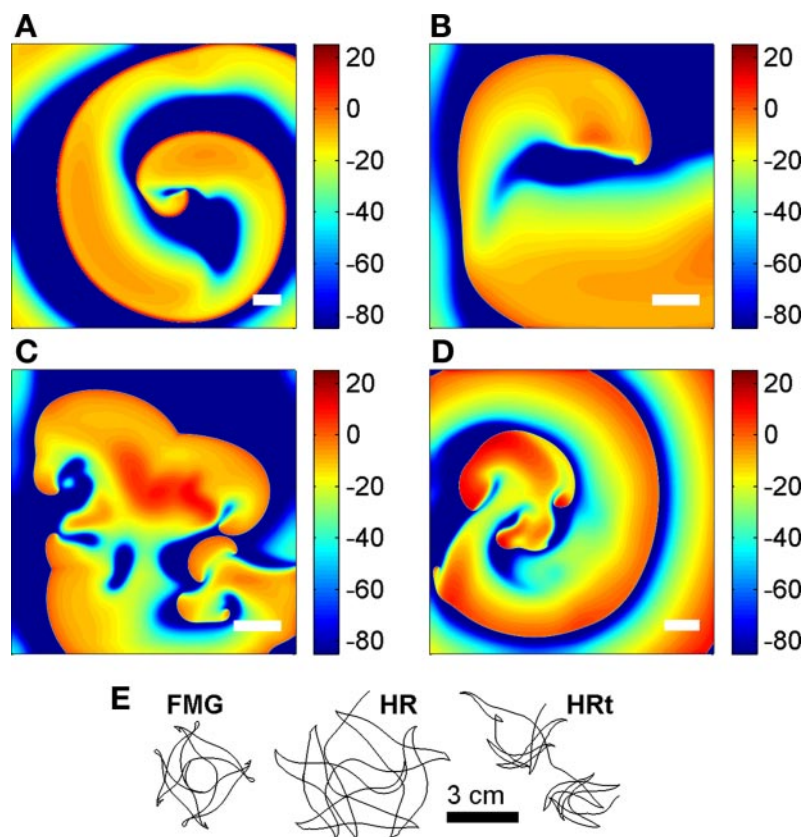


Fig. 7. Spiral wave dynamics of the FMG, HR, and HRT models. *A*: spiral wave initiated in the FMG model with an S1-S2 protocol in a large spatial domain (30 cm  $\times$  30 cm) produces transient breakup but ultimately stabilizes with a rotating linear core pattern. Time is 5 s with  $\Delta t = 0.02$  ms and  $\Delta x = 0.0125$  cm. *B–C*: with the HR model, a spiral wave initiated with an S1-S2 protocol in a large domain may rotate stably with a widely meandering linear core (*B*) or may break up into multiple waves (*C*). The S2 stimulus in *C* was applied 30 ms earlier, at 450 ms rather than at 480 ms, than in *B*; all other initial conditions were the same as in *B*. Domains are 18 cm  $\times$  18 cm and time is 2.8 s in both panels, with  $\Delta t = 0.01$  ms and  $\Delta x = 0.015$  cm. *D*: with the HRT model, quasi-breakup occurs, with a spiral wave often fractionating as it runs into refractory tissue but usually mending itself quickly. Domain size is 24 cm  $\times$  24 cm and time is 1.86 s, with  $\Delta t = 0.01$  ms and  $\Delta x = 0.015$  cm. Color bars show voltage (in mV) and all scale bars indicate 3-cm lengths. *E*: representative tip trajectories corresponding to *A*, *B*, and *D*. Trajectories were taken after transient breakup had terminated in the FMG simulation and during a relatively stable period of the HRT simulation. *D* = 0.001 cm<sup>2</sup>/s in all cases.

ms. The dominant period of the HR model when stable (179 ms) was larger than during breakup (162 ms). The HRT model was in between these two, with a dominant period of 168 ms.

#### HUMAN VENTRICULAR CELL MODELS

Disagreement between models of the same species and region is not specific to models of canine ventricular electrophysiology. Two human ventricular models (38, 43) similarly have different properties (21, 44). The Priebe-Beuckelmann (PB) model (38) describes human epicardial ventricular myocytes using 17 variables, 10 transmembrane currents, and intracellular calcium handling based on Ref. 35. The ten Tusscher et al. (TNNP) model (43) describes human epicardial, endocardial, and midmyocardial myocytes using 17 variables, 12 transmembrane currents, and intracellular calcium handling with intracellular calcium dynamics based on Ref. 13. Although the model includes descriptions for endocardial and M cells, here we refer only to the epicardial model settings to better match the PB model. In both cases, human data were used to develop expressions for  $I_{Kr}$ ,  $I_{Ks}$ ,  $I_{to}$ ,  $I_{K1}$ , and  $I_{Ca}$ . The TNNP also used human data for  $I_{Na}$ . Other currents in both models were based largely on those of Ref. 35. Despite the use of similar underlying data for most currents, the models' differing formulations of transmembrane currents and intracellular calcium handling generate APs of different lengths (Fig. 8, *A* and *B*) with different rate dependence (21, 44). In two dimensions, these differences give rise to different reentrant spiral wave dynamics. The PB model exhibits quasi-stability with a hypermeandering, largely linear core (Fig. 8, *C* and *E*) (21). The TNNP model, in contrast, produces a stable spiral with a linear core (Fig. 8, *D* and *E*) (21, 44).

#### HUMAN ATRIAL CELL MODELS

Another example with more dramatic differences can be seen in two models of human atrial cells (14, 36). The Nygren et al. (NFFCLCG) model (36) describes human atrial myocytes using 29 variables, 12 transmembrane currents, two-compartment SR calcium handling, dyadic cleft ionic concentrations, and extensive buffering. The Courtemanche-Ramirez-Nattel (CRN) model (14) has 21 variables, expressions for the same 12 transmembrane currents, and calcium handling based closely on Ref. 35, with a two-compartment sarcoplasmic reticulum and buffering. The models are based largely on the same human studies for  $I_{Na}$ ,  $I_{to}$ ,  $I_{Kur}$  [referred to as sustained outward current ( $I_{sus}$ ) in Ref. 36 but derived from similar data as  $I_{Kur}$  in Ref. 14],  $I_{Ca}$ ,  $I_{Kr}$ ,  $I_{Ks}$ , and  $I_{K1}$ , while using different previous models as the basis for the remaining currents and intracellular calcium handling (see Ref. 31 for the NFFCLCG and Ref. 35 for the CRN). The resulting models give extremely different behavior. For example, the NFFCLCG model produces triangular-shaped APs at all CLs (Fig. 9*A*), whereas the CRN model has APs with spike-and-dome morphology at long CLs (Fig. 9*B*) that become triangular only at short CLs (10, 37). The main adaptation to rate of the CRN model is a shortening of APD (only a slight change in RMP), whereas the main adaptation to rate of the NFFCLCG model is an increase in RMP (only slight APD shortening) (10). In tissue, these models also generate opposite results: the NFFCLCG model remains completely stable for longer than 60 s, with a small circular core about 2 cm in diameter (Fig. 9, *C* and *E*), whereas the CRN model is generally quasi-stable (Fig. 9, *D* and *E*), with a predominantly linear meandering tip trajectory and quickly

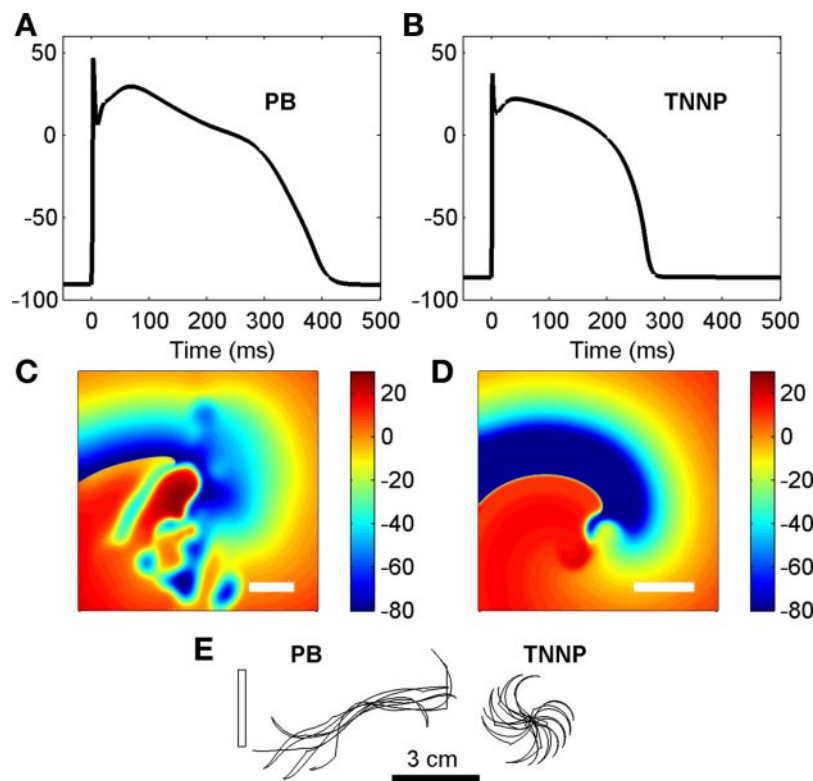


Fig. 8. Properties of two human ventricular cell models. *A*: Priebe-Beuckelmann (PB) model action potential at a CL of 1,000 ms. This model has a pronounced notch and biphasic repolarization. *B*: ten Tusscher (TNNP) model (Ref. 43) AP at a CL of 1,000 ms. The APD of this model is 100 ms shorter than that of the PB model for this CL. *C*: in the PB model, initiated spiral waves experience frequent wavefront fractionation but heal quickly, usually within tens of milliseconds. Domain size is 16 cm  $\times$  16 cm and time is 3.16 s, with  $\Delta x = 0.02$  cm and  $\Delta t = 0.01$  ms. *D*: in the TNNP model, initiated spiral waves are stable with a slowly precessing linear core. In smaller domains, breakup can be more persistent due to interactions with boundaries, although the activity usually self-terminates. Domain size is 12 cm  $\times$  12 cm and time is 21.28 s, with  $\Delta x = 0.02$  cm and  $\Delta t = 0.02$  ms. *E*: Representative tip trajectories corresponding to *C* and *D*. Trajectories were taken during a relatively stable period of the PB simulation and after stabilization of the trajectory in the TNNP simulation. Color bars show voltage (in mV) and all scale bars indicate 3-cm lengths.

healing wave breaks, similar to the dynamics of the HRT and PB models (10). The quasi-stability of the CRN model is maintained in sufficiently large tissues, although it is capable of supporting multiple waves, especially when its meandering core (hypermeandering, with linear petals approximately 3–4 cm long) interacts with domain boundaries in smaller tissue sheets (10).

## DISCUSSION

One possible explanation for disagreement among models of the same species and region is natural electrophysiological heterogeneity. Different electrophysiological properties have been reported for cells in different locations in canine ventricular myocardium, including transmural (2, 5, 8, 32, 33), apex-base (42), and left-right (2, 15) differences in ion channel expression and AP properties. Other differences also occur naturally, including statistical variations from cell to cell as well as differences due to characteristics like age (29) and sex (46).

The canine ventricular models presented do not state that they represent cells of a particular age or sex, and they provide only transmural location information. The FMG model is stated to be a model of the midmyocardial cell, whereas the HR model is stated to be an epicardial model. However, the FMG model does not exhibit the substantial APD prolongation at slow rates that is characteristic of normal midmyocardial cells (1, 2, 5, 8, 32, 33), and because the conductance of  $I_{to}$  is large enough to create a significant notch, it does not appear to represent a normal endocardial cell either (2, 5, 8, 32, 33). These characteristics suggest that the properties of the FMG model actually may be closer to epicardial cells. If so, the two models would be expected to share many properties.

Differences like location, age, and sex also are a possible explanation for differences in the human ventricular and atrial

models. In fact, when compared with the canine and human ventricular models, the human atrial models perhaps have reason to reflect the strongest electrophysiological heterogeneity. The human atria have been reported to exhibit strong remodeling with age, including an increase in heterogeneity (3). In addition, pronounced regional differences in ion channel expression and, consequently, AP morphology have been observed in the canine right atrium (17). If similar differences are present in human atria, combined with right-left and sex-based differences in channel expression, there is reason to believe that the two human atrial models, despite possessing very different properties, may represent naturally occurring heterogeneity.

However, another explanation is possible: the models may accurately reproduce the dynamics associated with the data on which they are based, but the underlying electrophysiology may not be known with enough accuracy over a broad enough range of physiological conditions to allow robust modeling. For instance, the canine ventricular models may reproduce the transmembrane currents whose descriptions are based on canine ventricular data, but the extension of other current descriptions and intracellular calcium handling from other models not specific to the same species and region of the heart may not be a good enough approximation and may cause the model to give invalid results when the dynamics of these systems are critically important. In addition, most models are not validated against AP data from short CLs, alternans dynamics in single cells and in tissue, and spiral wave dynamics. If the models are not robust enough because the underlying data on which they are based is not known over a broad range of conditions, the models cannot be assumed to have predictive power beyond the range of conditions and properties against which they were validated.

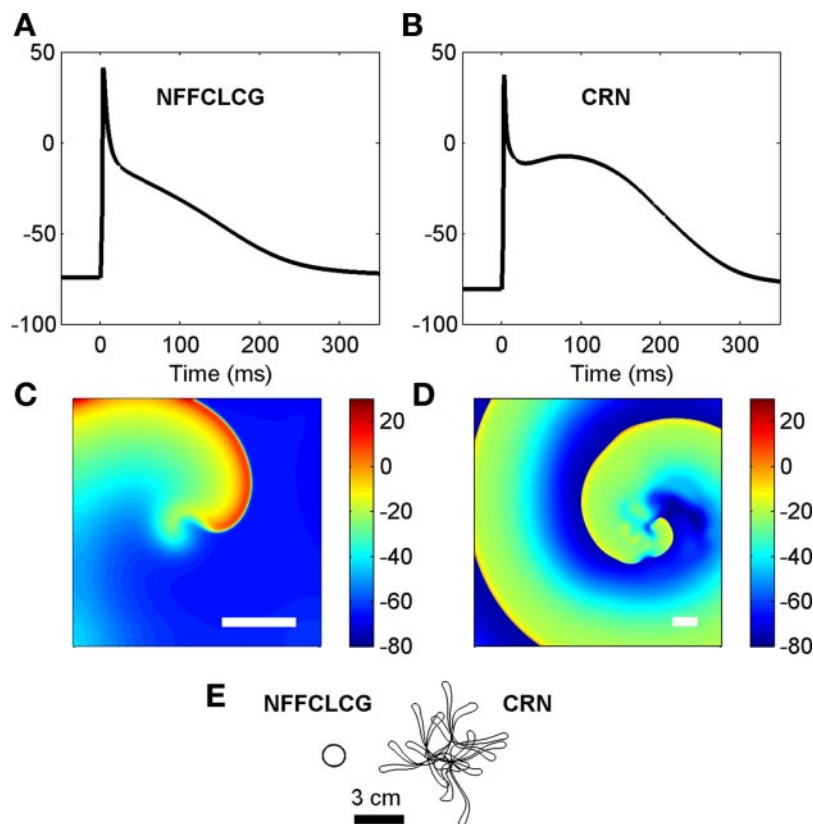


Fig. 9. Properties of two human atrial cell models. *A*: Nygren et al. (NFFCLCG) model (Ref. 36) AP at a CL of 1,000 ms. This model produces triangular APs at all CLs with limited rate adaptation. *B*: Courtemanche-Ramirez-Nattel (CRN) model AP at a CL of 1,000 ms. This model produces spike-and-dome APs at long CLs, with AP shortening and triangular morphology at short CLs. *C*: in the NFFCLCG model, an initiated spiral wave is stable, rotating around a circular core. Domain size is 10 cm  $\times$  10 cm and time is 60 s, with  $\Delta x = 0.025$  cm and  $\Delta t = 0.01$  ms. *D*: in the CRN model, an initiated spiral wave in a large domain undergoes transient breakup that usually heals quickly (within tens of ms). Breakup occasionally produced a small number of additional wavefronts. In smaller domains, breakup can be more persistent due to interactions with boundaries, although the activity usually self-terminates. Domain size is 30 cm  $\times$  30 cm and time is 19.4 s, with  $\Delta x = 0.01$  cm and  $\Delta t = 0.02$  ms. *E*: representative spiral tip trajectories corresponding to *C* and *D*. The CRN trajectory was taken during a relatively stable period of the simulation. Color bars show voltage (in mV) and all scale bars indicate 3-cm lengths.

The possibility that models may not be robust enough to represent dynamics outside a certain range of conditions has serious implications for the usefulness of models. Many models are developed to represent isolated myocytes and are not validated against tissue dynamics, where differences are known to exist (32) and can affect dynamics (11). In addition, a model may have been validated for specific conditions, but it may not remain valid for different conditions, which can include different cell locations, age, and sex as well as pacing rate and environmental conditions like temperature and external ionic concentrations. Changing the model parameters to match some aspects of different experimental data does not ensure that the original validation holds, unless additional verification that the altered model matches important characteristics of the original model is performed. Another potential complication is that parameter values may not always be known with great accuracy, but a model formulation may be quite sensitive to some of these parameters. A good example of this sensitivity is the FMG model, where simply increasing the conductance of  $I_{Kr}$  by a factor of two does not modify the restitution properties by much but eliminates alternans in a single cell (22). However, in tissue the alternans reappears, and reentry under these conditions is destabilized, resulting in sustained breakup in two dimensions compared with the stable reentry obtained for the original model (11, 12).

Overall, the more complicated the model, with large numbers of variables and parameters, the less predictable the behavior over a broad range of conditions. With enough parameters, it is possible to create a model that possesses a certain property. However, demonstrating that a model and an experiment have a common property does not mean that the same mechanism produces that

property in both cases. For instance, modeling studies have shown that at least three distinct mechanisms can produce alternans in cardiac tissue: steep restitution (25), alternans in intracellular calcium cycling (41), and electrotonic currents in the ischemic border zone (4), and without further experimental verification it cannot be known which mechanism is responsible for alternans in a given species and region of the heart under specific experimental conditions.

Given these caveats, the main utility of cardiac electrophysiological models is not in providing explanations of as yet unverified dynamics but in offering testable hypotheses regarding the mechanisms responsible for specific properties. Ideally, there should be an interplay between experiments and models: models are based on experimental data, but they should inspire further experiments to test their predictions, and those experiments should suggest refinements to the models. Although models may forecast certain types of behavior under specific conditions, further experimental work always will be needed for verification. Until such validation is performed, model predictions must be treated as applicable only to the specific model and physiological conditions used to generate them.

The choice of which model to use for a given computational study will depend on the question of interest. At a minimum, the model chosen must possess the properties to be studied, but the study may not require as many details about other aspects. Simple models at times may be useful for testing hypotheses concerning the range of possible behaviors, but detailed models of ion channels often will be necessary to address other issues, such as the effects of channel-blocking pharmacological agents. Many times there may not be an obvious "best model" to use for a given computational study. Modelers can make it easier to understand

both the advantages and the limitations of their models by discussing both in detail and by ensuring that all equations, parameter values in self-consistent units, and initial conditions necessary to code the model are included. If possible, a working code should be included in an online repository associated with the first publication of a model, and any corrections to published equations or parameter values should be identified subsequently in errata or corrigenda that are linked electronically with the online publication. Finally, because of the differences among models, results should be qualified as pertaining to the specific species, heart region, and conditions modeled, and studies should specify over what ranges of physiological conditions the results are expected to be valid.

## ACKNOWLEDGMENTS

We gratefully thank Dr. R. F. Gilmour, Jr. for teaching us the art and science of microelectrode recordings and for useful discussions. We also thank Dr. Y. Rudy for useful discussions.

## REFERENCES

1. Antzelevitch C, Shimizu W, Yan GX, Sicouri S, Weissenburger J, Nesterenko VV, Burashnikov A, Di Diego J, Saffitz J, Thomas GP. The M cell: its contribution to the ECG and to normal and abnormal electrical function of the heart. *J Cardiovasc Electrophysiol* 10: 1124–1152, 1999.
2. Antzelevitch C, Fish J. Electrical heterogeneity within the ventricular wall. *Basic Res Cardiol* 96: 517–527, 2001.
3. Anyukhovsky EP, Sosunov EA, Chandra P, Rosen TS, Boyden PA, Danilo P Jr, Rosen MR. Age-associated changes in electrophysiologic remodeling: a potential contributor to initiation of atrial fibrillation. *Cardiovasc Res* 66: 353–363, 2005.
4. Arce H, Xu A, Gonzalez H, Guevara MR. Alternans and higher-order rhythms in an ionic model of a sheet of ischemic ventricular muscle. *Chaos* 10: 411–426, 2000.
5. Baláti B, Varró A, Papp JG. Comparison of the cellular electrophysiological characteristics of canine left ventricular epicardium, M cells, endocardium and Purkinje fibres. *Acta Physiol Scand* 164: 181–190, 1998.
6. Beeler GW, Reuter H. Reconstruction of the action potential of ventricular myocardial fibres. *J Physiol* 268: 177–210, 1977.
7. Bondarenko VE, Szigeti GP, Bett GC, Kim SJ, Rasmusson RL. Computer model of action potential of mouse ventricular myocytes. *Am J Physiol Heart Circ Physiol* 287: H1378–H1403, 2004.
8. Burashnikov A, Antzelevitch C. Differences in the electrophysiologic response of four canine ventricular cell types to  $\alpha_1$ -adrenergic agonists. *Cardiovasc Res* 43: 901–908, 1999.
9. Cabo C, Boyden PA. Electrical remodeling of the epicardial border zone in the canine infarcted heart: a computational analysis. *Am J Physiol Heart Circ Physiol* 284: H372–H384, 2003.
10. Cherry EM, Fenton FH, Hastings HM, Evans SJ. Differences in reentry dynamics between two human atrial cell models (Abstract). *Pacing Clin Electrophysiol* 26: 985, 2003.
11. Cherry EM, Fenton FH. Suppression of alternans and conduction blocks despite steep APD restitution: electrotonic, memory and conduction velocity restitution effects. *Am J Physiol Heart Circ Physiol* 286: H2332–H2341, 2004.
12. Cherry EM, Gilmour RF Jr, Fenton FH. Tissue dynamics of two models of canine ventricular cell electrophysiology: restitution, memory, and reentry properties (Abstract). *Heart Rhythm* 3: S227, 2006.
13. Chudin E, Goldhaber Garfinkel A J, Weiss J, Kogan B. Intracellular  $Ca^{2+}$  dynamics and the stability of ventricular tachycardia. *Biophys J* 77: 2930–2941, 1999.
14. Courtemanche M, Ramirez RJ, Nattel S. Ionic mechanisms underlying human atrial action potential properties: insights from a mathematical model. *Am J Physiol Heart Circ Physiol* 275: H301–H321, 1998.
15. Di Diego JM, Sun ZQ, Antzelevitch C.  $I_{to}$  and action potential notch are smaller in left vs. right canine ventricular epicardium. *Am J Physiol Heart Circ Physiol* 271: H548–H561, 1996.
16. DiFrancesco D, Noble D. A model of cardiac electrical activity incorporating ionic pumps and concentration changes. *Philos Trans R Soc Lond B Biol Sci* 307: 353–398, 1985.
17. Feng J, Yue L, Wang Z, Nattel S. Ionic mechanisms of regional action potential heterogeneity in the canine right atrium. *Circ Res* 83: 541–551, 1998.
18. Fenton F, Karma A. Vortex dynamics in three-dimensional continuous myocardium with fiber rotation: filament instability and fibrillation. *Chaos* 8: 20–47, 1998.
19. Fenton FH, Evans SJ, Hastings HM. Memory in an excitable medium: a mechanism for spiral wave breakup in the low excitable limit. *Phys Rev Lett* 83: 3964–3967, 1999.
20. Fenton FH, Cherry EM, Hastings HM, Evans SJ. Multiple mechanisms of spiral wave breakup in a model of cardiac electrical activity. *Chaos* 12: 852–892, 2002.
21. Fenton FH, Bueno Orovio A, Evans SJ, Hastings HM, Cherry EM. Reentrant arrhythmias in human ventricular models (Abstract). *Heart Rhythm* 3: S186, 2006.
22. Fox JJ, McHarg JL, Gilmour RF Jr. Ionic mechanism of electrical alternans. *Am J Physiol Heart Circ Physiol* 282: H516–H530, 2002.
23. Fox JJ, Bodenschatz E, Gilmour RF Jr. Period-doubling instability and memory in cardiac tissue. *Phys Rev Lett* 89: 138101, 2002.
24. Goldhaber JI, Xie LH, Duong T, Motter C, Khuu K, Weiss JN. Action potential duration restitution and alternans in rabbit ventricular myocytes: the key role of intracellular calcium cycling. *Circ Res* 96: 459–466, 2005.
25. Guevara MR, Ward G, Shrier A, Glass L. Electrical alternans and period doubling bifurcations. *Comput Cardiol* 167–1670, 1984.
26. Hund TJ, Kucera JP, Otani NF, Rudy Y. Ionic charge conservation and long-term steady state in the Luo-Rudy dynamic cell model. *Biophys J* 81: 3324–3331, 2001.
27. Hund TJ, Rudy Y. Rate dependence and regulation of action potential and calcium transient in a canine cardiac ventricular cell model. *Circulation* 110: 3168–3174, 2004.
28. Iyer V, Mazhari R, Winslow RL. A computational model of the human epicardial myocyte. *Biophys J* 2004: 1507–1525, 2004.
29. Jeck CD, Boyden PA. Age-related appearance of outward currents may contribute to developmental differences in ventricular repolarization. *Circ Res* 71: 1390–1403, 1992.
30. Koller ML, Riccio ML, Gilmour RF Jr. Dynamic restitution of action potential duration during electrical alternans and ventricular fibrillation. *Am J Physiol Heart Circ Physiol* 275: H1635–H1642, 1998.
31. Lindblad DS, Murphey CR, Clark JW, Giles WR. A model of the action potential and underlying membrane currents in a rabbit atrial cell. *Am J Physiol Heart Circ Physiol* 271: H1666–H1691, 1996.
32. Liu DW, Gintant GA, Antzelevitch C. Ionic bases for electrophysiological distinctions among epicardial, midmyocardial, and endocardial myocytes from the free wall of the canine left ventricle. *Circ Res* 72: 671–687, 1993.
33. Liu DW, Antzelevitch C. Characteristics of the delayed rectifier current ( $I_{Kr}$  and  $I_{Ks}$ ) in canine ventricular epicardial, midmyocardial, and endocardial myocytes. *Circ Res* 76: 351–365, 1995.
34. Luo CH, Rudy Y. A model of the ventricular cardiac action potential. Depolarization, repolarization, and their interaction. *Circ Res* 68: 1501–1526, 1991.
35. Luo C, Rudy Y. A dynamic model of the cardiac ventricular action potential. *Circ Res* 74: 1071–1096, 1994.
36. Nygren A, Fiset C, Firek L, Clark JW, Lindblad DS, Clark RB, Giles WR. Mathematical model of an adult human atrial cell: the role of  $K^+$  currents in repolarization. *Circ Res* 82: 63–81, 1998.
37. Nygren A, Leon LJ, Giles WR. Simulations of the human atrial action potential. *Phil Trans R Soc Lond A* 359: 1111–1125, 2001.
38. Priebe L, Beuckelmann DJ. Simulation study of cellular electric properties in heart failure. *Circ Res* 82: 1206–1223, 1998.
39. Rosen MR. What is cardiac memory? *J Cardiovasc Electrophysiol* 11: 1289–1293, 2000.
40. Shannon TR, Wang F, Puglisi J, Weber C, Bers DM. A mathematical treatment of integrated Ca dynamics within the ventricular myocyte. *Biophys J* 87: 3351–3371, 2004.
41. Shiferaw Y, Watanabe MA, Garfinkel A, Weiss JN, Karma A. Model of intracellular calcium cycling in ventricular myocytes. *Biophys J* 85: 3666–3686, 2003.
42. Szentadrassy N, Banyasz T, Biro T, Szabo G, Toth BI, Magyar J, Lazar J, Varro A, Kovacs L, Nanasi PP. Apico-basal inhomogeneity in distribution of ion channels in canine and human ventricular myocardium. *Cardiovasc Res* 65: 851–860, 2005.

43. **Ten Tusscher KHWJ, Noble D, Noble PJ, Panfilov AV.** A model for human ventricular tissue. *Am J Physiol Heart Circ Physiol* 286: H1573–H1589, 2004.
44. **Ten Tusscher KHWJ, Bernus O, Hren R, Panfilov AV.** Comparison of electrophysiological models for ventricular cells and tissues. *Prog Biophys Mol Biol* 90: 326–345, 2006.
45. **Watanabe MA, Fenton FH, Evans SJ, Hastings HM, Karma A.** Mechanisms for discordant alternans. *J Cardiovasc Electrophysiol* 12: 196–206, 2001.
46. **Xiao L, Zhang L, Han W, Wang Z, Nattel S.** Sex-based transmural differences in cardiac repolarization and ionic-current properties in canine left ventricles. *Am J Physiol Heart Circ Physiol* 291: H570–H580, 2006.
47. **Zhang H, Holden AV, Kodama I, Honjo H, Lei M, Varghese T, Boyett MR.** Mathematical models of action potentials in the periphery and center of the rabbit sinoatrial node. *Am J Physiol Heart Circ Physiol* 279: H397–H421, 2000.
48. **Zhao X, Schaeffer DG.** Alternate pacing of border-collision period-doubling bifurcations. *Nonlinear Dynamics*. In press.

